Journal of Marine Research, 72, 445–475, 2014

Circulation and cross-shelf transport in the Florida Big Bend

by Austin C. Todd[1], Steven L. Morey[2], and Eric P. Chassignet[3]

ABSTRACT

The Florida Big Bend region in the northeastern Gulf of Mexico contains both spawning sites and nursery habitats for a variety of economically valuable marine species. One species, the gag grouper (*Mycteroperca microlepis*), relies on the shelf circulation to distribute larvae from shelf-break spawning grounds to coastal sea-grass nurseries each spring. Therefore, identifying the dominant circulation features and physical mechanisms that contribute to cross-shelf transport during the springtime is a necessary step in understanding the variation of the abundance of this reef fish. The mean circulation features and onshore transport pathways are investigated using a numerical ocean model with very high horizontal resolution (800–900 m) over the period 2004–2010. The model simulation demonstrates that the mean springtime shelf circulation patterns are set primarily by flow during periods of southeastward or northwestward wind stress, and that significant cross-shelf flow is generated during southeastward winds. Lagrangian particle tracking experiments demonstrate that a primary pathway exists south of Apalachicola Bay by which particles are able to reach inshore, and that significantly more particles arrive inshore when they originate from an area adjacent to a known gag spawning aggregation site. The results provide, for the first time, a description of the pathways by which onshore transport is possible from gag spawning sites at the shelf break to sea-grass nurseries at the coast in the Florida Big Bend.

Keywords. Coastal circulation, ocean modeling, larval transport, gag grouper, Florida Big Bend

1. Introduction

The Florida Big Bend region (BBR) in the northeastern Gulf of Mexico (GOM) is located at the juncture of the Florida Peninsula and the Florida Panhandle, where the coastline orientation changes by roughly 90°. The sea-grass meadows along the coastline and the numerous reefs across the BBR provide both nursery habitats and spawning sites for a variety of marine species. The ecologically diverse and economically productive marine ecosystems of the BBR have been studied in relation to local fisheries (i.e., Hood and

1. Department of Marine, Earth and Atmospheric Sciences, North Carolina State University, Raleigh, NC, 27695. ***e-mail: actodd@ncsu.edu***

2. Center for Ocean-Atmospheric Prediction Studies, The Florida State University, Tallahassee, FL 32306-2840. ***e-mail: smorey@fsu.edu***

3. Center for Ocean-Atmospheric Prediction Studies, The Florida State University, Tallahassee, FL 32306-2840. ***e-mail: echassignet@fsu.edu***

Schlieder 1992; Koenig and Coleman 1998; Koenig et al. 2000; Gentner 2009). The physical oceanographic state can affect reef fish recruitment by setting egg and larval dispersion patterns and by influencing food availability (Rothschild and Osborn 1988; Werner et al. 1997). For example, ocean currents have been surmised to be the dominant mechanism responsible for the horizontal dispersion of fertilized eggs and planktonic larvae (Norcross and Shaw 1984). Currents can also affect the distribution of nutrient-laden, high-chlorophyll coastal waters (Morey, Dukhovskoy, and Bourassa 2009) and drive nutrient fluxes from the deep ocean (He and Weisberg 2003). Therefore, the shelf circulation can directly influence the recruitment and year-class strength of given species by moving fish eggs and larvae to or from areas that are conducive for survival (Norcross and Shaw 1984).

The ocean circulation on continental shelves is driven by a combination of local surface forcing, tides, rivers, and deep-ocean fluxes near the shelf break. However, the dominant forcing mechanism on the West Florida Shelf (WFS) and Florida Panhandle Shelf is the local wind stress (Clarke and Brink 1985; Mitchum and Clarke 1986; Morey and O'Brien 2002; Morey, Zavala-Hidalgo, and O'Brien 2005; Weisberg et al. 2005). From late fall through spring, the winds over the BBR are dominated by synoptic events associated with the passage of cold fronts. The strength, duration, and frequency of these frontal winds vary interannually, when some years have stronger or more frequent frontal passages. The differences in shelf circulation patterns and upwelling from year to year can be largely attributed to the interannual differences in the strength and duration of upwelling-favorable wind events (Weisberg and He 2003).

Understanding the impact of oceanic transport on reef fish recruitment is crucial for effective fisheries management (Fitzhugh et al. 2005). Commercial and recreational fishing causes reductions in both adult fish abundance and juvenile fish populations in the GOM, and recreational fishing accounts for more than 60% of annual landings of certain fish species (Coleman et al. 2004). Although fishing pressures can affect population size, population-independent processes that occur during egg, larval, and early juvenile stages are significant in determining the interannual variability in fish recruitment (Rothschild 1986; Chambers and Trippel 1997). Among these processes is the transport of eggs, larvae, and early juveniles by the ocean currents.

The gag grouper (*Mycteroperca microlepis*) relies on the circulation for transport of its eggs and larvae during the pelagic stage of its early life cycle (Keener et al. 1988; Koenig and Coleman 1998; Fitzhugh et al. 2005). Gag are among the most valuable finfish in the region, estimated to provide more than $100 million in value added and more than $60 million in income to the southeastern United States from recreational fishing alone (Gentner 2009). Adult gag form spawning aggregations along offshore reefs near the continental shelf break (50–100 m depth) from January to April, with peak spawning in February and March (Hood and Schlieder 1992; Coleman, Koenig, and Collins 1996; Koenig et al. 2000; Fitzhugh et al. 2005). Their larvae spend 30–60 days (mean ~43 days) in the water column before settlement in the coastal sea grasses some 70–600 km away (a period known as their pelagic larval duration) (Koenig and Coleman 1998; Fitzhugh et al. 2005). The vertical positions

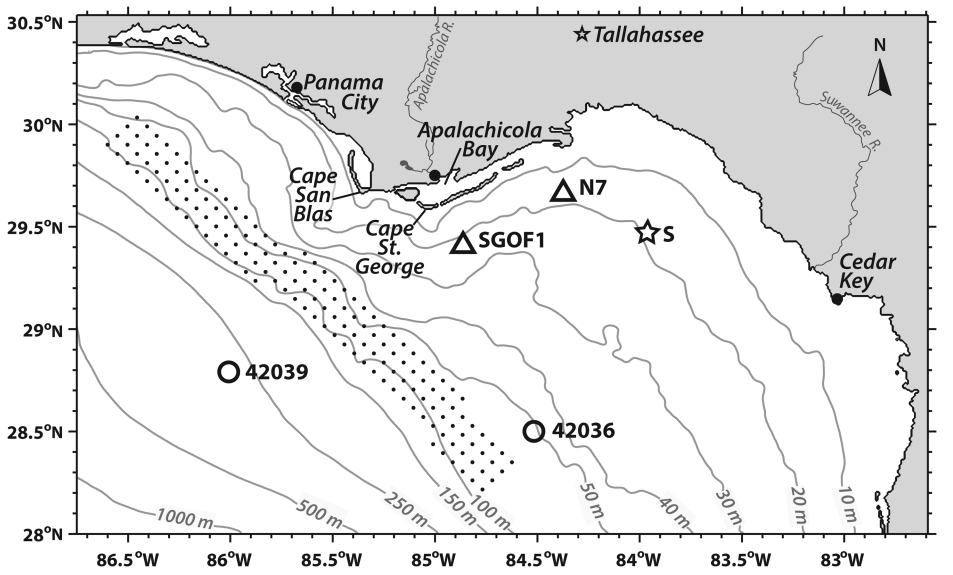

Figure 1. Florida Big Bend region (BBR) and the BBR configuration of the Regional Ocean Modeling System modeling domain. Triangles represent observational towers, open circles represent National Data Buoy Center buoys, closed circles represent coastal sea-level stations, dots depict particle seeding locations, and the star denotes the location of the current profiler at site S.

of gag larvae in the water column and their behavior during this stage of development are not fully understood. Keener et al. (1988) found evidence of a diel vertical migration in conjunction with tidal phase near barrier island inlets in South Carolina. However, it is unclear if gag exhibit the same vertical migration farther offshore. Furthermore, the smaller tidal amplitudes and tidal residual currents in the BBR shelf may play a lesser role in the nearshore transport of gag in the BBR (He and Weisberg 2002a; Gouillon et al. 2010). Estimating the onshore transport mechanisms for gag larvae in the BBR using an empirical model based on surface drifters and winds by Fitzhugh et al. (2005) proved to be unsuccessful, and they suggested that a fully three-dimensional approach is needed in order to understand the physical transport processes in the region.

Circulation studies in the BBR have included short-lived observations (i.e., Marmorino 1983a, 1983b; Weatherly and Thistle 1997), single-station time series (i.e., Weatherly and Thistle 1997; Maksimova and Clarke 2013), or those focused on general dynamics of the WFS (Mitchum and Sturges 1982; Mitchum and Clarke 1986; Yang and Weisberg 1999; Weisberg and He 2003; Weisberg et al. 2005). However, with such a unique bathymetry in the BBR, one cannot simply apply theory applicable to a long wide shelf such as the southern part of the WFS to the region. The BBR undergoes a dramatic transition from the very wide WFS (150–200 km wide) to the narrow Florida Panhandle Shelf (40 km at its narrowest point). This transition occurs offshore of Cape San Blas and Cape St. George, where the isobaths converge and undergo tight curvature (Fig. 1). The change in coastline orientation

in the BBR makes it a dynamically interesting area because there does not always exist a clear relationship between the along-isobath current and the along-isobath component of the wind stress here (Marmorino 1983a).

This study uses a high-resolution nested ocean modeling approach to understand the general dynamics governing circulation across the BBR and the cross-shelf transport during the spring months that may be important for transport of reef fish larvae spawned on the shelf edge. The model simulation is compared with a suite of regional observations, and the mean circulation features are described along with their variability. Analysis of the model results provides a description of the physical mechanisms by which cross-shelf transport is possible in the BBR and indicates the preferred pathways by which materials arrive inshore. The coastal circulation is found to respond barotropically to large-scale, low-frequency variations in the wind stress in conjunction with atmospheric frontal passages, which generate oscillations between phases of northwestward- and southeastward-directed wind stresses. The shelf circulation responds asymmetrically to the oscillating winds, resulting in a residual mean flow that is directed across shelf in the area with the tightest bathymetric curvature. The primary pathway for onshore transport exists to the southeast of Cape St. George, and a preferred origin for materials to successfully arrive inshore coincides with a known gag spawning aggregation.

2. The ocean model

The Regional Ocean Modeling System (ROMS; Shchepetkin and McWilliams 2003, 2005) is configured with a uniform 1/120° (∼800–925 m) horizontal grid spacing that extends north of 28° N and east of 86.75° W to the Florida coastline (see Fig. 1). ROMS is a free-surface, terrain-following, primitive equation ocean model that is frequently used for shelf and coastal applications (Shchepetkin and McWilliams 2005). The terrain-following vertical s-coordinate of ROMS provides a constant 30 vertical grid layers at density points on an Arakawa C grid (31 layer interfaces at $w$points), with stretching of the s-coordinate layers that provides higher resolution at the surface and near the bottom. Grid spacing is more evenly distributed in depths shallower than ∼100 m; the constant number of vertical layers effectively increases the overall vertical resolution of the model over shallower depths.

Although the nonalignment of the vertical coordinate isosurfaces to isopycnals or geopotential surfaces may lead to spurious diapycnal mixing or errors in association with the calculation of the horizontal pressure gradient (Marchesiello, McWilliams, and Shchepetkin 2001; Lemarié et al. 2012), advanced advection schemes are used in ROMS to limit these errors. The BBR configuration of ROMS (henceforth BBROMS) uses a third-order, upstream-biased advection scheme for momentum with a specifically designed predictor-corrector time step algorithm. This allows the generation of physically realistic steep gradients in the prognostic variable fields (Shchepetkin and McWilliams 1998). Advection of tracers is computed using the multidimensional positive definite advection transport algorithm, which reduces numerical overshoots and spurious diapycnal mixing by use of

a flux-corrector scheme (Smolarkiewicz 1984). The horizontal pressure gradient is calculated using a vertical spline reconstruction of the density field (Shchepetkin and McWilliams 2003), and the Mellor-Yamada 2.5 turbulence closure scheme is used with an improved stability function (Mellor and Yamada 1974, 1982; Kantha and Clayson 1994). The frictional bottom boundary stress is calculated using a quadratic bottom drag formulation with a nondimensional drag coefficient set to 0.003. The BBROMS topography uses the National Geodetic Data Center's 30-arc-second coastal relief data set, to which a uniform Gaussian filter with a radius of 3 grid points is applied. Smoothing of steep gradients in the topography is done to satisfy suggested grid stiffness ratios related to the calculation of horizontal pressure gradient ($rx_0 < 0.35$ and $3 \leq rx_1 \leq 7$; Haney 1991; Beckman and Haidvogel 1993; Sikirić, Janeković, and Kuzmić 2009). The smoothing of the topography and the choice of numerical schemes reduce potential errors caused by the calculation of the horizontal pressure gradient.

The model's initial conditions and temporally evolving open boundary conditions are provided by the 1/25° Gulf of Mexico Hybrid Coordinate Ocean Model (GOM HYCOM; Bleck 2002; Chassignet et al. 2007, 2009; Chassignet 2011). HYCOM is forced at the surface using the Navy Operational Global Atmospheric Prediction System and uses the Navy Coupled Ocean Data Assimilation system (Cummings 2005) to assimilate available satellite altimeter observations, satellite and in situ sea surface temperatures, and in situ vertical temperature and salinity profiles from Expendable bathythermographs, Argo floats, and moored buoys. The GOM HYCOM experiment used for this study does not include tidal forcing. HYCOM's state-of-the-art prediction system provides a robust estimate of the ocean state that is well resolved in space and time and may be applied as boundary conditions to the higher-resolution BBROMS (Barth, Alvera-Azcárate, and Weisberg 2008a, 2008b; Chassignet et al. 2009).

The initial conditions on 1 January 2004 and the boundary conditions are prescribed using the temperature, salinity, sea surface height, and velocity fields from the GOM HYCOM (available as daily snapshots at 00:00 UTC) and are interpolated to the BBROMS grid using splines in the vertical and horizontal. The interpolated GOM HYCOM fields are then applied at the open boundaries using radiation conditions and with a nudging term that is imposed at the boundary and over a transition zone near the boundary. The model field over the transition zone is then adjusted to be a weighted combination of the initially computed BBROMS field and the field set by the GOM HYCOM. For example, the equation of the predicted fields has a term such as

$$\frac{\partial A}{\partial t} = \cdots + T_{\text{nudge}}(A - A_0), \tag{1}$$

where A is the predicted value of temperature, salinity, sea level, or velocity from BBROMS; A_0 is the corresponding field from the GOM HYCOM; and T_{nudge} is a relaxation timescale that follows the formula

$$T_{\text{nudge}} = \frac{1}{\tau}\exp(-x/15), \tag{2}$$

where $\tau = 10$ days and x is the number of grid cells away from the boundary. The associated relaxation timescale for T_{nudge} ranges from 0.1 days at the boundary to 10 days at 44 grid cells ($\sim$35 km or roughly the internal radius of deformation) away from the boundary. Beyond the boundary relaxation zone, $T_{nudge} = 0$. Flather boundary conditions are applied to the two-dimensional momentum variables normal to the boundaries, and Chapman boundary conditions are applied to the free surface to allow for gravity wave radiation (Flather 1976; Chapman 1985).

Nineteen rivers provide fluxes of momentum and low-salinity water at the coast. River stream flows are prescribed using daily means from U.S. Geological Survey gauges and are applied as sources of constant low salinity (3 practical salinity units [PSU]). River temperatures vary as monthly climatology values, and stream flows are applied as linear profiles in the vertical, which allows a higher percentage of outflow at the surface.

The BBROMS is forced at the surface using output from the Climate Forecast System Reanalysis (CFSR). The CFSR, a global coupled ocean/atmosphere/land/sea ice–modeling system that uses the National Centers for Environmental Prediction Global Data Assimilation System, is described in great detail in Saha et al. (2006). The CFSR's output fields are provided in the form of analysis fields every 6 hours, with hourly forecast fields for the intermediate time steps. The horizontal resolution of the CFSR is roughly 1/3°. ROMS uses 10 m winds, air temperature, specific humidity, pressure, rainfall, and shortwave and longwave radiation to calculate momentum, heat, and freshwater fluxes via bulk formulae adapted from the Coupled Ocean-Atmosphere Response Experiment (COARE; see Fairall et al. 2003). Atmospheric pressure is used to calculate the surface fluxes in ROMS, but it is not directly used to force sea-level variations.

BBROMS hindcast simulations are initialized from the GOM HYCOM on 1 January 2004 and run continuously for the period 2004–2010. After $\sim$2 weeks from the model start, high-frequency fluctuations in the model's total kinetic energy (indicative of gravity wave radiation from initial adjustment) disappear, indicating that adjustment from the interpolated HYCOM fields used for initialization to the high-resolution grid/topography and surface forcing occurs rapidly.

3. Big Bend circulation

The following section provides a description of the mean flow features of the BBR. First, the veracity of the ocean model simulation is evaluated through comparison with regional observations. Then, the mean springtime flow features are described. Finally, the variability of the flow is discussed on various timescales, providing a description of the major components of the BBR circulation.

a. Model validation

The ocean model simulation is compared with a suite of regional observations from coastal sea-level gauges, surface buoys, and bottom-mounted current profilers. Three coastal sea-level gauges are located within the model domain at Cedar Key, Apalachicola, and Panama City. Surface temperatures are available from buoys 42036 and 42039 and tower SGOF1. Finally, the model velocities are compared with two current profiler time series at site N7 and site S (Fig. 1). Observed and modeled sea levels and currents are filtered to subinertial frequencies using a cosine-Lanczos filter (consistent with Maksimova and Clarke [2013]), which passes 50% power at a frequency of $2\pi/40$ hours. Lunar and solar fortnightly tides are removed from observed sea-level and current measurements using a least squares fit before applying the filter. Unless specifically noted otherwise, correlations are significant at the 95% confidence interval (P value ≤ 0.05) according to a standard Student's t-test.

i. Sea level. The simulated sea-level anomalies are compared with data from three coastal tide gauge stations operated by the NOAA Center for Operational Oceanographic Products and Services. Observed sea-level anomalies are referenced to their 1981–2001 mean, and the simulated sea-level anomalies are referenced to the simulation-long mean (1 January 2004 to 31 December 2010) and are barometrically adjusted to account for atmospheric pressure variations. The BBROMS simulation reproduces observed coastal sea-level anomaly variations well, with maximum springtime correlations of 0.88 for Panama City (Fig. 2), 0.84 for Apalachicola, and 0.92 for Cedar Key (see Table 1 for complete statistics). The springtime root mean squared error (rmse) falls below 6.2 cm at Panama City and Cedar Key (8.6 cm at Apalachicola), with the exception of 2010, when the model simulation has a bias toward lower sea-level anomalies with rmse values that increased by 18%–44%. This year was a warm El Niño/Southern Oscillation (ENSO)–phase year (an El Niño year). Warm-phase ENSO years are subject to increased atmospheric cyclogenesis over the GOM compared with years with near-neutral or cold ENSO phases, due to the positioning of 300 hPa jets over the GOM and a shift of the Bermuda High well eastward of the continental United States (Smith et al. 1998; Kennedy et al. 2007). This increases the occurrence of cyclones that progress eastward across the GOM and, consequently, increases the frequency of low-sea-level events over the eastern GOM (Kennedy et al. 2007). The variability of the modeled sea level remains highly correlated with the observed sea-level anomalies during 2010, with correlations greater than 0.92, 0.86, and 0.93 for Panama City, Apalachicola, and Cedar Key, respectively.

ii. Temperature. The model accurately reproduces surface temperatures at regional buoy observations, where comparisons of temperature data taken every 3 hours at buoy sensor depth ($\sim$0.7 m below the sea surface) indicate that the correlation exceeds 0.97 (P value $=$ 0) and the linear regression fit falls very close to the unity line (see Table 2). This is evident in the unfiltered time series of surface temperature at buoy 42036 for spring 2004 (Fig. 3),

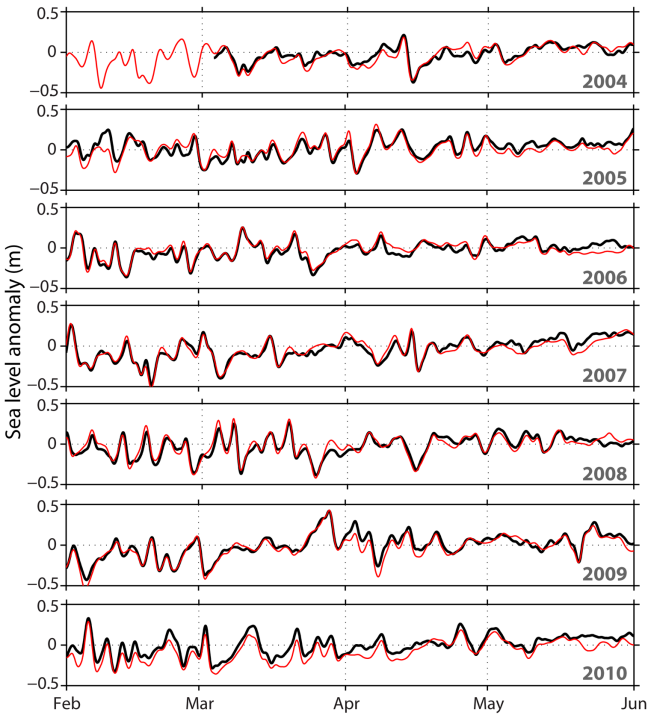

Figure 2. Modeled (red) and observed (black) springtime subinertial sea-level anomalies near Panama City, Florida. Model sea levels have been barometrically adjusted to account for atmospheric pressure variations. Modeled sea levels for 2004, 2005, and 2007–2009 are plotted at a lag of −3 hours to demonstrate high correlations.

Table 1. Comparison of coastal sea level to tide gauge observations at three locations in the BRR. The model and observations have been filtered following procedures outlined in the text.

Location	Correlation	Lag (hours)	*P* value	$\sigma_{model}/\sigma_{obs}$	rmse (cm)
Apalachicola	0.84	−4	0	1.01	8.6
Cedar Key	0.92	−1	0	1.00	6.1
Panama City	0.89	0	0	1.04	6.0

where the rmse is 0.77°C and the model almost always falls within the range of instrument error. Although the model does have a warm bias during spring 2004, Figure 3 shows that the model captures the 7- to 10-day synoptic-scale variability of near-surface temperature well. Similar fits are seen at the other buoys in the region, as indicated by the close regression fits seen in Table 2.

Table 2. Linear regression parameters for SST (°C) from the BBROMS simulation fit to moored buoy observations. Intercepts are on the y-axis (predicted SSTs from the linear regression fit of the model to observations)

Location	Slope	Intercept	Correlation
42036	1.00	−0.16	0.97
42039	1.02	−0.16	0.95
SGOF1	1.02	−0.69	0.98

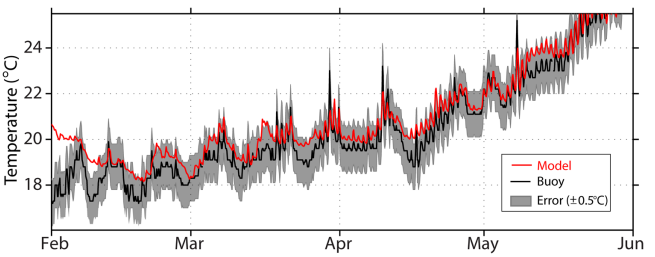

Figure 3. Water temperature (°C) near buoy sensor depth (∼0.7 m below the sea surface) at National Data Buoy Center buoy 42036 location during February–May 2004. The red line indicates predicted model temperature, the black line indicates the observed temperature, and the gray shaded area encompasses the possible range of observed temperatures based on the instrument's 0.5°C measurement accuracy.

iii. Currents. Modeled velocities are compared with observed velocities from two bottom-mounted current profilers at depths of 19 m southeast of Apalachicola Bay at site N7 and at site S (Fig. 1). These observations are the only available in situ velocity measurements in the region over the time period of interest, and Maksimova and Clarke (2013) describe their seasonal and interannual variability in detail. A bottom-mounted acoustic Doppler current profiler (ADCP) was deployed at site N7 on 19 January 2007, and a bottom-mounted acoustic wave and current (AWAC) profiler was deployed at site S from 23 April 2009 to 9 July 2010. The bottom-mounted ADCP has a blanking distance of 4 m, and measurements are averaged into 1 m vertical bins. Surface data contamination occurs in the uppermost 3 m, and therefore, velocities in this surface layer are removed and unused in the analysis. The velocities observed using the AWAC are resolved in 1 m bins from 1 m above the bottom (mab) to 16 mab, roughly 3 m below the surface. The data record for site N7 covers 96% of the period from deployment to 8 October 2010, and only a very small gap exists between deployments at site S during November 2009 (resulting in 97% coverage).

Maksimova and Clarke (2013) provide a detailed analysis of the observed velocities at site N7 and site S across multiple seasons. Their work demonstrates that most of the subinertial energy of the currents lies in the synoptic band (periodicity of 3–15 days), and that the subinertial along-isobath flow at both sites is proportional to the component of the wind

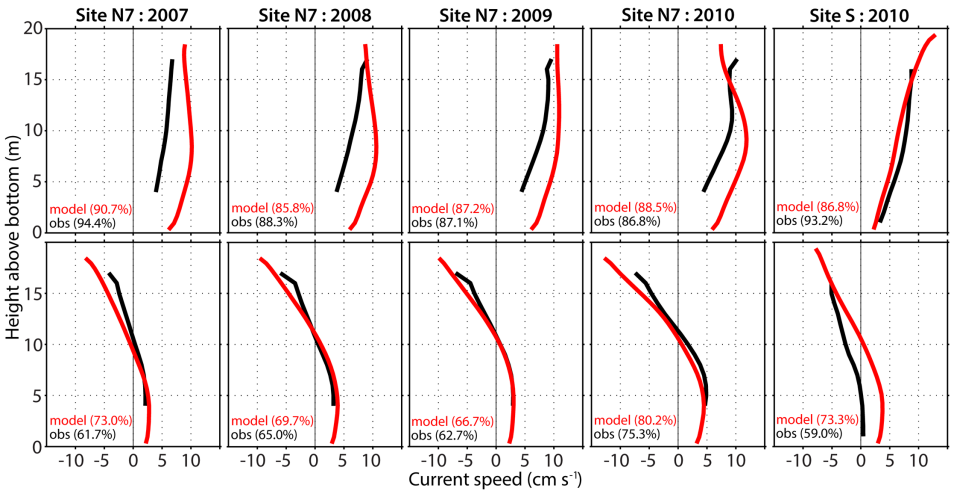

Figure 4. Vertical structure of the first-mode empirical orthogonal functions (EOFs) for springtime modeled (red) and observed (black) along-isobath (top) and cross-isobath (bottom) currents at site N7 and site S. The explained variance of the first-mode EOF is indicated in the parentheses. EOFs are scaled by the standard deviation of their principal component to allow for comparison with actual speeds.

stress oriented along the WFS. In addition, the ocean's response to this large-scale, low-frequency forcing is largely independent of depth (as demonstrated through the first-mode empirical orthogonal functions [EOFs]). Maksimova and Clarke (2013) indicate a strong relationship between the depth-averaged, subinertial velocities and the synoptic-scale wind stress.

In similar fashion to the data processing used by Maksimova and Clarke (2013), observed velocities at site N7 and site S are processed by first removing lunar and fortnightly tides using a least squares fit. Modeled and observed velocities are then filtered to subinertial frequencies and are rotated to along-isobath and cross-isobath components, where the along-isobath and cross-isobath axes are defined as the semimajor and semiminor axes of the standard deviation ellipse for depth-averaged flow, respectively (see Fig. 4 in Maksimova and Clarke [2013] for a depiction of the ellipses at each site). The rotational axes are calculated independently for each data set and for the model simulation but differ in orientation by less than 5°.

The mean springtime currents at each depth are weak and can be an order of magnitude smaller than their standard deviation. The first-mode EOFs of along-isobath flow at site N7 and site S (which explain ∼90% of the variance, see Fig. 4) show the vertical structure to be relatively independent of depth, except for a weakening of the currents in the bottom 8–9 m (consistent with the vertical turbulent frictional length scale) (Marmorino

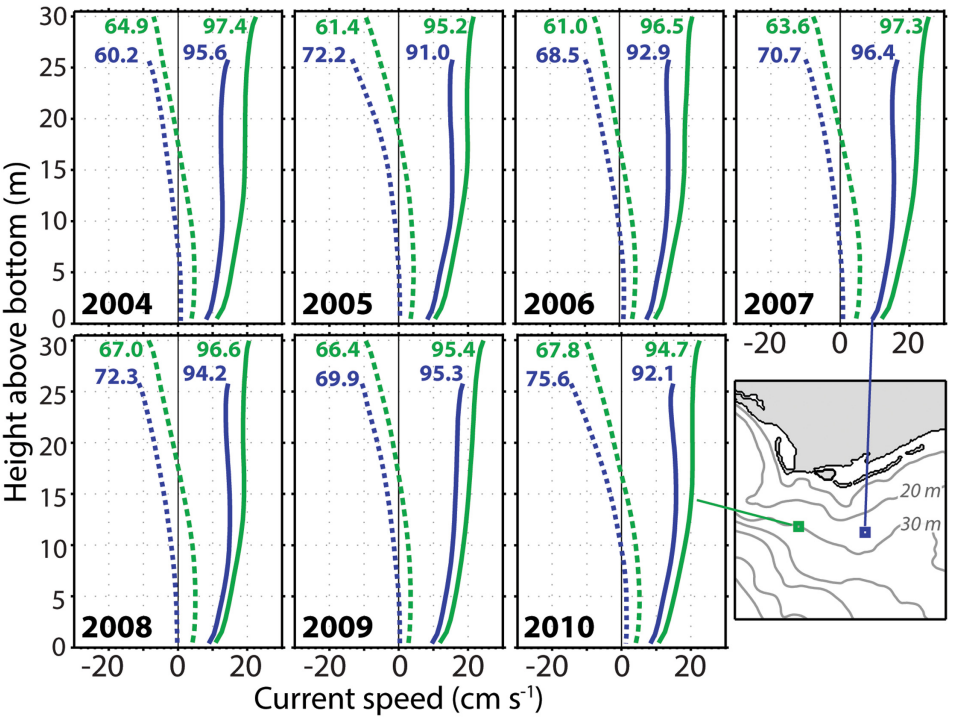

Figure 5. Vertical structure of the first-mode empirical orthogonal functions (EOFs) for springtime modeled currents at two locations south of Cape St. George. Solid lines denote along-isobath flow (positive with shallower isobaths to the left), and dashed lines denote cross-isobath flow (positive onshore). The explained variance of the first-mode EOF is indicated next to its corresponding line. EOFs are scaled by the standard deviation of their principal component to allow for comparison with actual speeds.

1983b; Maksimova and Clarke 2013). Current speeds decrease in the surface turbulent frictional layer in 2010 at N7, which may be attributed to enhanced surface Ekman flow that opposes the along-isobath flow (Maksimova and Clarke 2013). Indeed, Maksimova and Clarke (2013) found that by adding a term to the along-isobath flow that approximates the Ekman flow in 2010, the shear within the surface turbulent frictional layer is reduced. The vertical structure of the modeled along-isobath currents agrees well with the observations at these two sites, although the model tends to overestimate the magnitude of the currents in the bottom half of the water column. To the southwest of N7 and in slightly deeper water, the model demonstrates nearly barotropic structure of the springtime velocities (Fig. 5). In this region, the first-mode EOFs of along-isobath currents explain up to 97% of the variance. The currents during all years are stronger here than at site N7 and site S, and they exhibit less of a reduction in the surface turbulent layer in 2010, indicating that the shallower depths

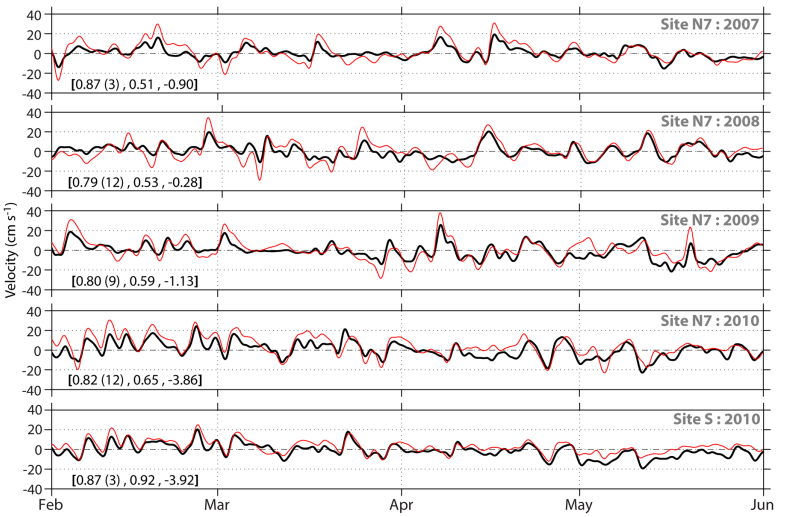

Figure 6. Modeled and observed depth-averaged springtime along-isobath currents at site N7 and site S (bottom panel for 2010). Values in the triplet indicate the maximum correlation R at the hour lag indicated in parentheses, regression slope, and mean model error (in cm s^{-1}). Modeled velocities are plotted at the lags indicated in parentheses to demonstrate the high correlations.

or complex bathymetry near N7 may play more of a role in inducing shear into the currents there.

The depth-averaged springtime flow is dominated by variations in the along-isobath direction. The variance captured by the first-mode EOFs for cross-isobath currents are up to 35% lower than those of along-isobath currents (Figs. 4 and 5), which indicates that the first-mode EOFs may not as accurately represent the cross-isobath flow. This may be due to increased noise in the weaker cross-isobath velocities or the nonlinearity of the cross-isobath flow response (see Maksimova and Clarke 2013). The mean cross-isobath velocities at each depth are only $\sim$1 cm s^{-1} at site N7 and site S, and the cross-isobath EOFs demonstrate that velocities through most of the water column are generally less than half the strength of along-isobath currents. Although the vertical structure of the cross-isobath velocities is sheared (more so at site N7), the magnitudes of these currents are weaker than their along-isobath counterparts, and their vertical structure yields smaller and noisier depth-averaged currents. This is especially true along the 30 m isobaths south of Cape St. George, where the EOFs demonstrate that cross-isobath flow is nearly three times slower than the along-isobath flow (see Fig. 5), resulting in nearly barotropic structure. This is consistent with the idea that the depth-averaged flow here should be mostly along isobath.

Correlations between modeled depth-averaged along-isobath currents and the observed currents at site N7 and site S are near or exceed 0.8 for February–June, indicating that the variability of the observed springtime flow is captured well by the model (Fig. 6). The

depth-averaged flow is weaker at site S, and the overestimation of the stronger flow in 2010 is reduced here, whereas the correlation remains high ($R > 0.85$). The flow at site S should be weaker due to an alongshore pressure gradient brake set up by the sharp topographic changes near the Florida Keys (Maksimova and Clarke 2013).

The model reproduces the main variability present in the observations, and in some seasons, the model accounts for more than 75% of the variance seen in observed currents ($R > 0.86$). The remaining portion of the variance unaccounted for in the model could arise from many sources, and any model is inherently limited by its ability to accurately represent bottom friction and true bathymetric variability. Although the observational record at site N7 is the longer of the two current meters, the complex local bathymetry and proximity to several rivers provide challenges to model with extreme accuracy. Results are more promising at site S, where the geography is less complex. Furthermore, the BBROMS is dependent on the GOM HYCOM's representation of remotely generated forcing features (such as coastal trapped waves) at the BBROMS open boundaries. Any misrepresentation of remotely generated variability by HYCOM could contribute to the remaining variance that is unaccounted for in the BBROMS simulations. The following section explores the major characteristics of the mean springtime circulation across the entirety of the BBR in order to identify features that may contribute to transport away from the shelf break.

b. Mean shelf circulation features

A surface-to-middepth concentrated jet flows northwestward along the continental slope (offshore of the 150 m isobath; Fig. 7). This northwestward slope jet flows in the opposite direction to the jet proposed by Hetland et al. (1999) and observed further south by He and Weisberg (2003). However, it is consistent with average drift velocities of intermediate-depth drifters in the region (Weatherly, Wienders, and Romanou 2005), with the flow provided at the open boundaries by the GOM HYCOM, and although stronger in the BBROMS simulations, it flows in the same direction as the slope flow in the simplified WFS model presented by He and Weisberg (2002b). Because He and Weisberg (2002b) neglect Loop Current (LC) forcing during their study period of March–May, and Hetland et al. (1999) use a hypothetical LC setup, these studies are not able to fully capture the variability in LC position and extent. Therefore, the strong flow offshore of the shelf break is attributed to deep ocean fluxes set by the open boundary conditions (an idea that is consistent with that proposed by He and Weisberg [2003]).

Adjacent to this area of northwest flow along the slope, there is a distinct separation in flow patterns between the circulation on the shelf and the circulation over the continental slope and deep ocean. Between the two regions, the mean depth-averaged currents change direction by 180° across a narrow region of ~15–20 km at the shelf break. This is consistent with the finding by He and Weisberg (2003) that the deep ocean influences the shelf circulation only within a radius of deformation of the shelf break. Therefore, because this study is concerned with the wind-driven flow on the shelf and not the flow seaward of the

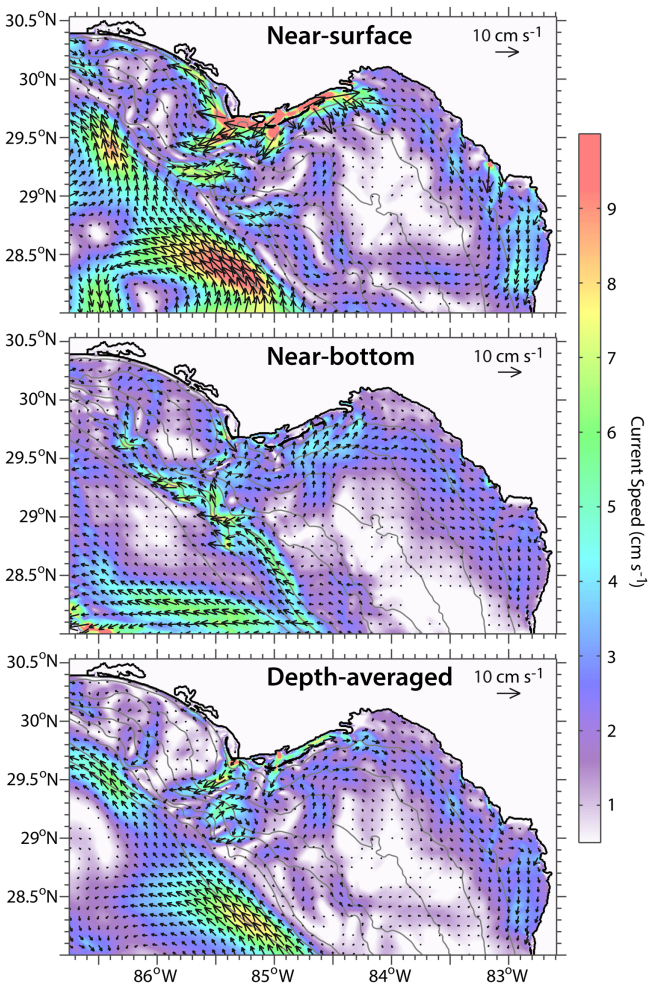

Figure 7. Seven-year mean springtime velocities from the Big Bend region configuration of the Regional Ocean Modeling System simulation. Velocity vectors are plotted every 10 grid points, and model bathymetry is contoured every 10 m until 50 m depth, then at depths of 75, 100, 200, 500, and 1,000 m.

shelf break, which is set mostly by the deep ocean, the following discussion focuses only on those features on the shelf.

Perhaps the most striking feature of the mean depth-averaged velocities is the area just offshore of Cape San Blas and Cape St. George. The mean flow in this area exhibits a banded structure of onshore currents juxtaposed with offshore currents, where the mean cross-shelf currents extend from the coastline to nearly the shelf break. These features are

observed in the depth-averaged velocity fields and at all depths. Inshore and eastward of this region, close to the barrier islands that separate Apalachicola Bay from the GOM, the mean flow in 10–15 m depth is cross isobath and vertically sheared, with opposing surface and bottom velocities directed offshore and onshore, respectively. The velocity shear is confined to within the 15 m isobath, which coincides with both the surface 32.5 PSU contour and the only area on the shelf where the squared Brunt-Väisäläa frequency exceeds 0.001 s^{-1}. The buoyant river water therefore contributes to the stratification inshore of the 15 m isobath and can lead to the associated velocity shear seen between near-surface and near-bottom currents in Figure 7. Beyond this region, there are no major fronts, and the flow direction is mostly depth independent.

Along the eastern portion of the BBR, the mean along-isobath flow within the 20 m isobath is directed toward the southeast at all depths. He and Weisberg (2003) describe a southeastward-flowing shelf jet that bifurcates at Cape San Blas into a shelf-break jet and a coastal jet. Although an organized southeast-directed coastal flow is seen in the mean springtime BBROMS simulation, a shelf-break component of this flow is very weak. The shelf-break component mostly vanishes immediately south of the region where He and Weisberg (2002b) indicate that a bifurcation occurs. However, the shelf-break flow that He and Weisberg (2002b) observe for March–May of 1999 is also very weak ($\sim$2 cm s^{-1}) and is approximately half the strength of the coastal flow. These speeds are consistent with those seen in the BBROMS simulations; however, the BBROMS simulations do not indicate a bifurcation of the flow south of Cape San Blas. The average velocities are very weak over nearly the entire midshelf in the widest portion of the BBR.

c. Flow variability

The dominant flow features described previously persist from year to year (Fig. 8), although the relative magnitudes of those flow features vary interannually. In particular, stronger cross-shelf flow offshore Cape San Blas and Cape St. George is observed in 2005, 2007, and 2010. Although these cross-shelf flow features are stronger in these years, it is in the onshore-flowing regions where the most distinct enhancement occurs; this is especially true south of Apalachicola Bay. The most pronounced flow enhancement occurs in 2010, when the mean shelf circulation features are stronger offshore of Cape San Blas and Cape St. George and along the coast. The northwestward slope jet is not nearly as prevalent in 2005 and 2010; it could be affected by the enhanced offshore extension of the shoreward flow south of Cape San Blas. In contrast to 2005, 2007, and 2010, the coastal jet vanishes in the spring mean for 2008 and 2009.

The dominant frequency of wind stress variability occurs at synoptic scales (3–10 days) during the spring season in association with the passage of atmospheric cold fronts. Westward winds are most frequent during spring months (28% of the springtime toward the southwest and 33% toward the northwest), as demonstrated by longer bars toward the west in the wind stress rose for the BBR (Fig. 9). Southeastward winds are less frequent (23% of the

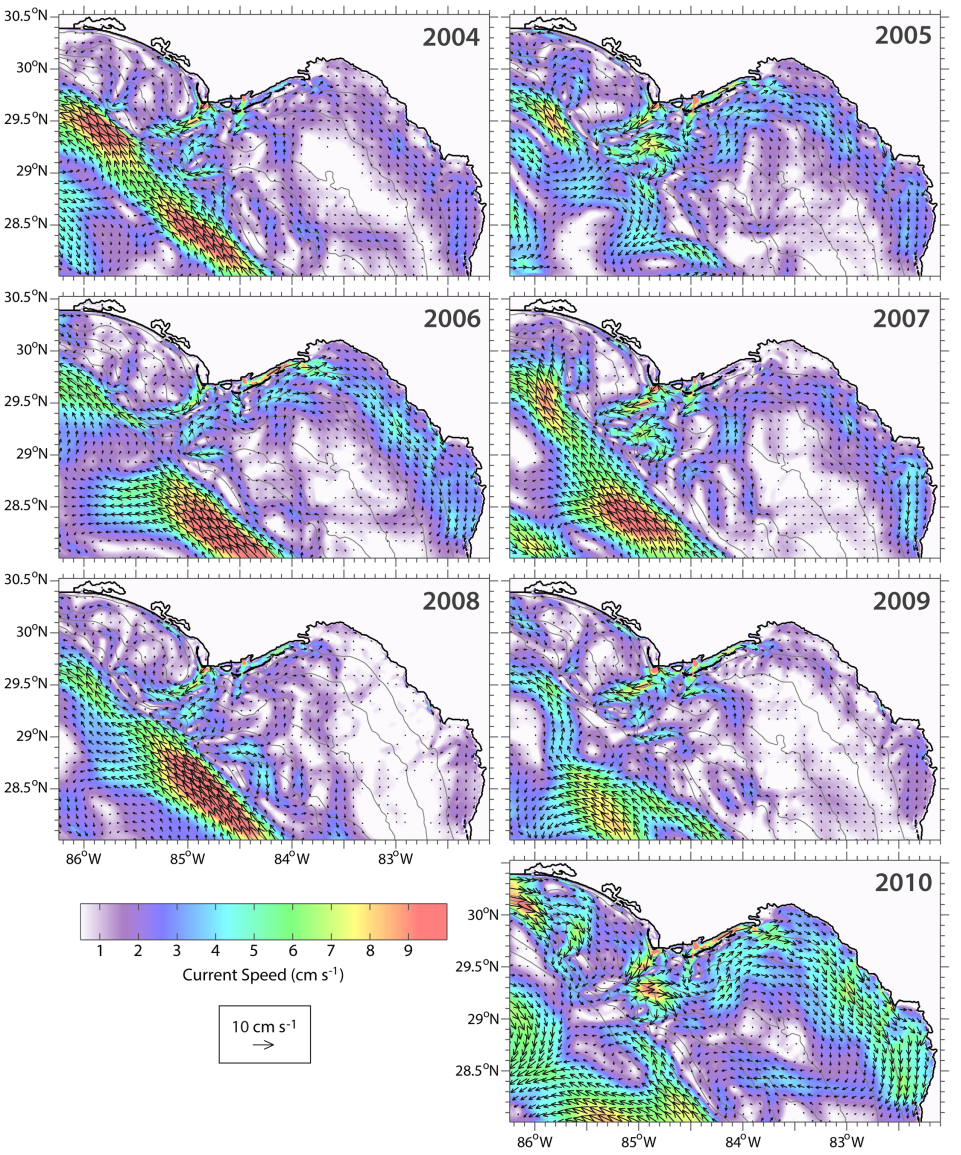

Figure 8. Similar to Figure 7, except for depth-averaged velocities averaged over each spring season.

time), yet are considerably stronger than winds in any other direction. Northeastward winds are both less frequent (occurring only 16% of the time) and weaker. The atmospheric frontal passages that dominate the variability of the springtime winds have typical prefrontal phases of northwestward winds and postfrontal phases of southeastward winds. By dissecting the

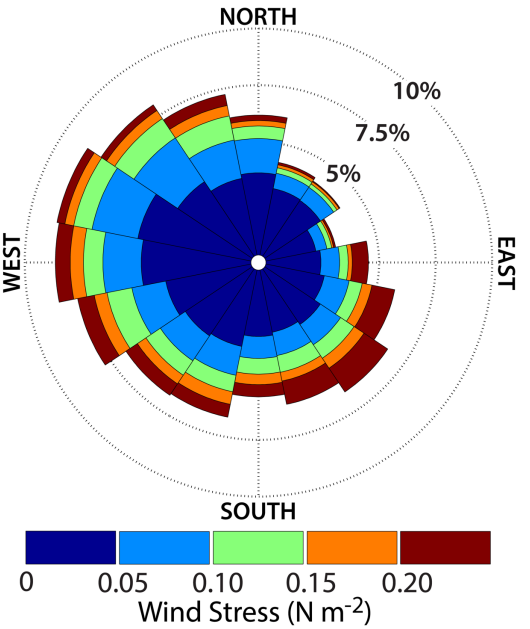

Figure 9. Wind stress roses for 2004–2010 spring months (February–May), calculated from the Big Bend region configuration of the Regional Ocean Modeling System simulation and from observations at National Data Buoy Center buoy 42036. Bars point in the direction from which the wind originates, and the lengths of the bars indicate the percentage of time that winds come from each direction. Different colors represent the range of wind stress magnitudes.

ocean circulation into flow during each of these two different wind regimes (i.e., averaging the spring velocities during northwestward winds or during southeastward winds), the two dominant flow patterns during the springtime circulation are captured (Fig. 10). Flow during southeastward winds (top panel of Fig. 10) yields a strong southeastward shelf flow that is enhanced offshore of Cape San Blas and Cape St. George (the area where cross-isobath flow occurs in Fig. 7). Flow during northwestward winds (middle panel of Fig. 10) features a weaker northwestward shelf flow and slope jet with stronger speeds over only one small region offshore of Cape San Blas. Over the midshelf, velocities during each wind regime are oriented along isobath but are of nearly equal speed and opposite orientation.

Averaging the flow during either southeastward or northwestward winds produces a depth-averaged flow field in which all of the features present in the full spring mean are retained (compare the bottom panels of Fig. 10 and Fig. 7). That is, the cross-shelf flow offshore of Cape San Blas and Cape St. George, the southeastward-flowing coastal jet, and the northwestward-flowing slope jet are each present in the conditionally averaged flows. Therefore, the cross-shelf velocities offshore Cape San Blas and Cape St. George

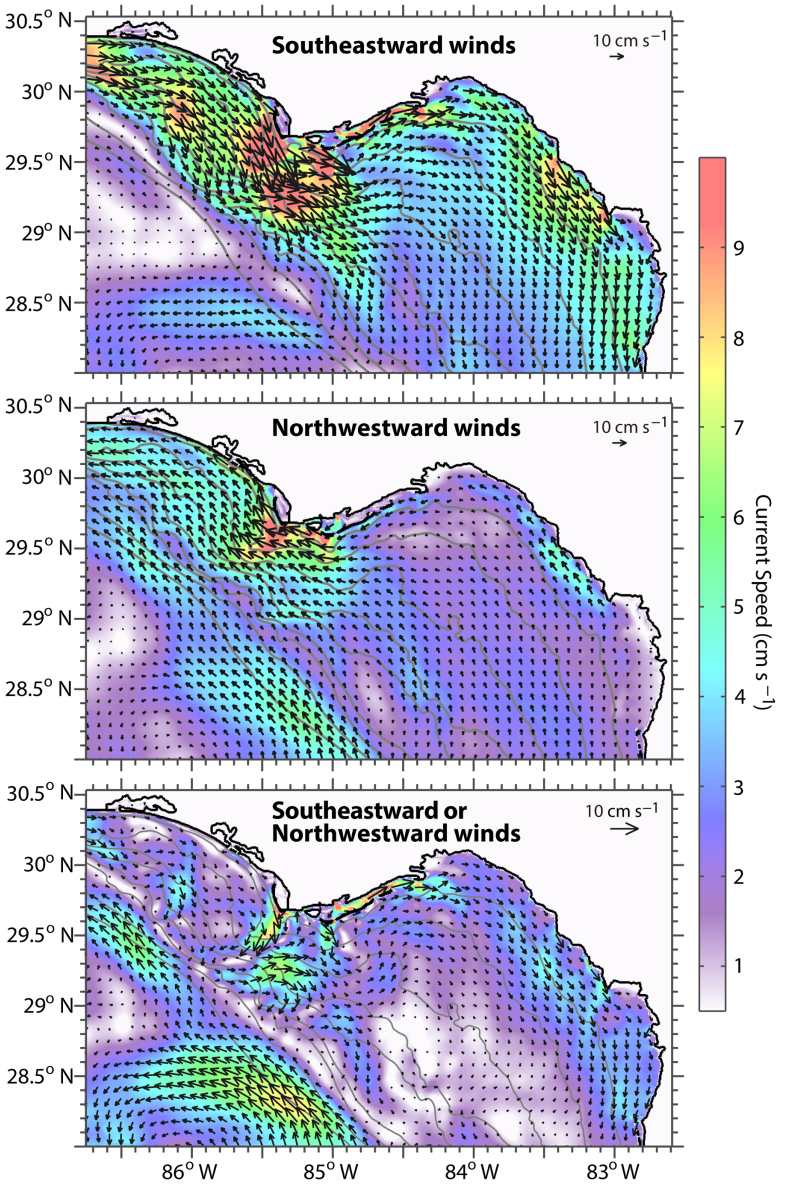

Figure 10. Depth-averaged spring velocities for the Big Bend region configuration of the Regional Ocean Modeling System simulation. Velocities from are conditionally averaged for springtime flow only during southeastward winds (top), northwestward winds (middle), and either southeastward or northwestward winds (bottom).

and the coastal jet are simply the residual of two asymmetric, yet opposite flows during oscillating southeastward and northwestward winds. The flow during southeastward winds is enhanced over the shoals extending from Cape San Blas and Cape St. George, and the same flow enhancement is not observed during northwestward winds. Therefore, the average over both of these wind regimes is directed cross isobath in this region, and the observed interannual variability in the strength of the flow features is a direct result of the variability in the synoptic-scale wind stress over the BBR. A similar residual flow occurs in the coastal jet, although the flow here is directed mostly along isobath during both wind regimes; it is simply the stronger flow during southeastward winds that prevails when averaging over both flow regimes.

What causes flow from one direction to cross isobaths, whereas flow from another direction follows isobaths? In the absence of friction, conservation of potential vorticity, $\frac{\zeta+f}{h}$, indicates that the flow should follow roughly along an isobath of depth h if the relative vorticity ζ is small compared the local Coriolis parameter f (i.e., $|\zeta|/f \rightarrow 0$). Cross-isobath movement is possible when $|\zeta|/f \rightarrow 1$. Scaling the relative vorticity as $\zeta \sim V/R_C$, where V is the current speed and R_C is the radius of curvature of the isobaths, indicates that the largest values of $\frac{|\zeta|}{f}$ occur during southeastward winds (Fig. 11), when the flow is strong ($|V|$ large) and isobaths tightly curve (R_C small) near Cape San Blas and Cape St. George. In this area, ζ is larger, and therefore, the potential vorticity contours are not aligned with contours of f/h (Fig. 11). However, northwestward flow here is weaker (with small $|V|$), such that $|\zeta|/f \rightarrow 0$ and the flow roughly follows contours of f/h. Therefore, the stronger flow during southeastward winds is more likely to cross isobaths in areas with tight bathymetric curvature. However, frictional effects, particularly in shallower waters and from strong wind forcing, will modify the potential vorticity of the system and may enable cross-isobath flow. The time over which the friction becomes important is related to the Ekman number (the ratio of the viscous forces to rotational forces) and is given by

$$\tau = E_V^{-1/2} f^{-1} = h\delta_E^{-1} f^{-1}, \tag{3}$$

where E_V is the Ekman number and δ_E is the Ekman layer depth (Pedlosky 1987) . Therefore, if $h = 20{-}100$ m, $\delta_E \sim 10$ m, and $f \sim 0.7 \times 10^{-5}\text{s}^{-1}$, this frictional "spin-down" time τ ranges from ~3 days on the inner shelf to 15 days on the outer shelf. Over timescales shorter than this, the flow can be expected to conserve potential vorticity. The following section demonstrates the contribution of the different circulation patterns and their variability to onshore transport.

4. Particle advection experiments

The larval transport Lagrangian model (LTRANS; see North et al. 2008; Schlag, North, and Smith 2008) is used to identify primary pathways for onshore transport of passive Lagrangian particles. With LTRANS, 156 passive Lagrangian particles are seeded every 3 hours for 12 weeks (104,832 particles per year) from predetermined release locations

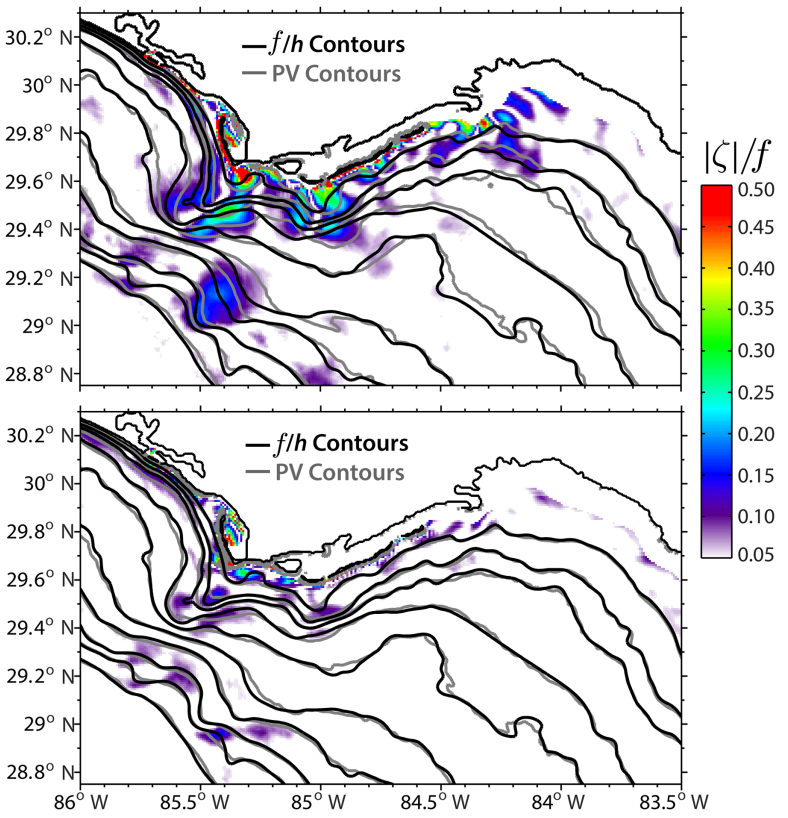

Figure 11. The ratio $|\zeta|/f$ for flow during southeastward winds (top) and during northwestward winds (bottom) is plotted in color, calculated from 7-year mean depth-averaged currents. Contours for both f/h and potential vorticity (PV) are drawn at 0.046×10^{-5}, 0.07×10^{-5}, 0.1×10^{-5}, 0.145×10^{-5}, 0.18×10^{-5}, 0.238×10^{-5}, 0.295×10^{-5}, 0.37×10^{-5}, 0.46×10^{-5}, and 0.7×10^{-5} m^{-1} s^{-1}.

between the 50 and 100 m isobaths (see release locations in Fig. 1), consistent with depths and locations where the gag grouper forms spawning aggregations. Particle seeding begins at 00:00 UTC on 1 February each year, and particles are advected by the depth-averaged BBROMS velocity field. An additional experiment has been run in which particles originate near the surface and bottom of the water column and are advected in the full three-dimensional velocity field. However, because that experiment yields nearly identical results to the one using depth-averaged velocities, it is not included in the current analysis. Each particle is followed for a maximum of 45 days, which corresponds to the mean gag pelagic larval duration (Fitzhugh et al. 2005). Particle trajectories are no longer followed once they reach the model boundaries.

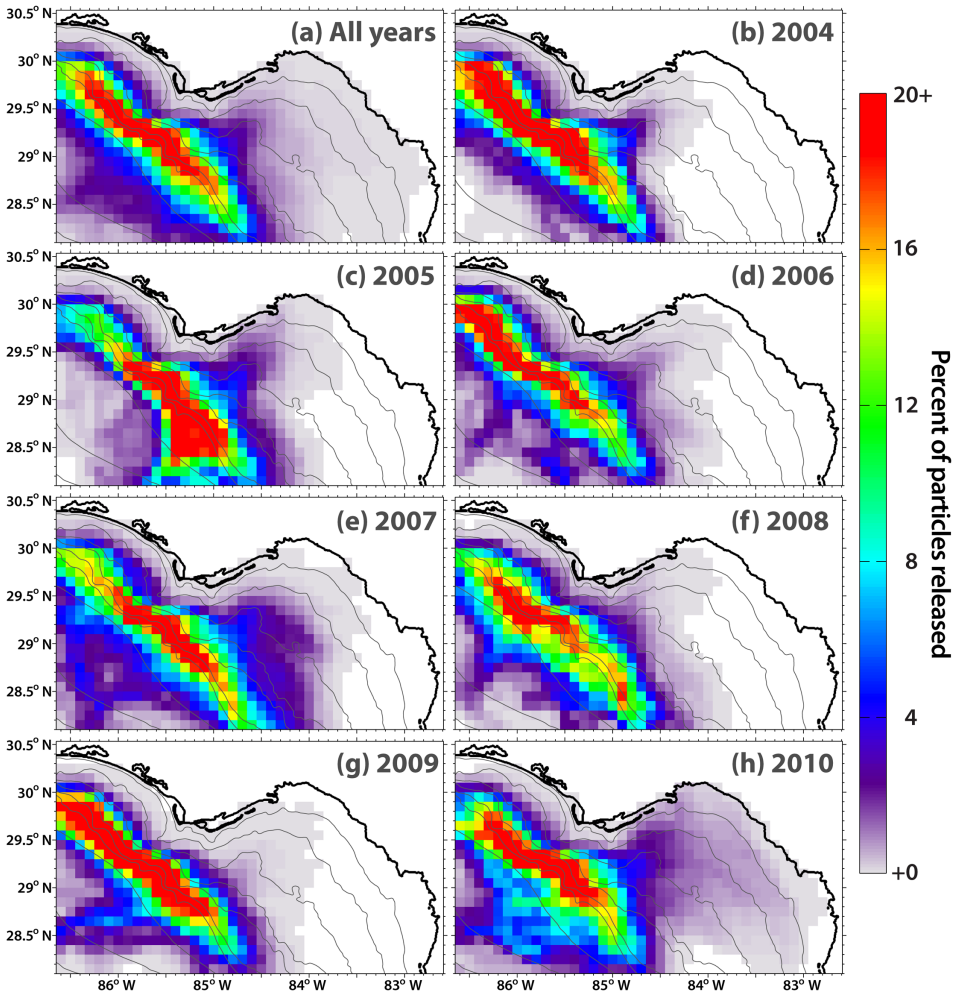

Figure 12. Particle track density for all particles released over the 7-year advection period (percentage of all 733,824 particles) (a) and calculated for each year (percentage of 104,832 particles released during that year) (b)–(h). Particles are advected in the depth-averaged Big Bend region configuration of the Regional Ocean Modeling System velocities. Model bathymetry is contoured every 10 m until 50 m depth, then at depths of 75, 100, 200, 500, and 1,000 m.

a. Particle track densities

The density of particle tracks (the percentage of particles to pass through $0.1^\circ \times 0.1^\circ$ spatial bins during their 45-day advection period) provides a metric to identify the preferred particle advection pathways (Fig. 12). The highest percentage of particles appears along the shelf break, reflecting both the particle deployment pattern in Figure 1 and their primary

transport pathway in the northwestward slope jet. It is evident that the slope jet provides the primary flow of particles, as the percentages are skewed toward higher values downstream of the jet in the northwest portion of the domain compared with lower values upstream near the southern boundary. Because of this northwestward flow, 39% of all particles leave the domain through the western boundary, whereas only 17% leave through the southern boundary. Therefore, the primary exit location is through the western boundary via the slope jet. The distribution of materials onto the shelf is then reliant on the southeastward winds and their ability to drive significant cross-shelf flow. However, few particles (~7,300 or 1%) arrive inshore of the 10 m isobath during their advection. Although an area of slightly higher particle track densities exists to the southeast of Cape St. George, the percentages in this area are less than 5% (Fig. 12a).

The distribution of particles advected toward the coast undergoes considerable interannual variability (Fig. 12b–h). In particular, the magnitude and extent of higher particle density southeast of Apalachicola Bay varies each year, with the highest percentages of particles in this region in 2005 and in 2010. A significant number of particles reach the inner shelf of the BBR in 2010; this is the only year when particles are spread over nearly the entire BBR, particularly along the midshelf to the southwest of Cedar Key. This region is generally void of particles in all other years, reinforcing its name as the "Forbidden Zone" (Yang et al. 1999). The shoreward tongue of higher particle densities to the southeast of Apalachicola Bay is significantly diminished in all other years from the levels seen in 2005 and 2010. During 2004 and 2006–2009, the percentage of particles advected inshore along the barrier islands of Apalachicola Bay is less than 5%. In 2007, a widely spread tongue of higher particle density is observed to the south of Cape St. George with percentages that are 3%–5% higher than observed in nonwarm-phase ENSO years (2004 and 2006–2009). However, this tongue is laterally spread toward the east over the midshelf rather than onshore. Years with higher particle track density in the area to the south of Apalachicola Bay are consistent with the years when the width and the strength of the cross-isobath flow features are enhanced in Figure 8, making the area a critical transit region for particles advected to the inner shelf.

b. Pathways for onshore transport

The primary pathways for onshore transport may be deciphered by examining the track density of only the 1% of particles that successfully reach the inner shelf at some point during their advection. The 10 m isobath is chosen as the inner shelf region because it provides a rough estimate of where sea grasses may occur in the BBR (the nursery habitat for juvenile gag grouper). The sea grasses exist in depths up to 20 m and at distances up to 50 km offshore (Iverson and Bittaker 1986; Thompson and Phillips 1987); however, their coverage is not always consistent or continuous, and they can be significantly affected by flood-stage river outflow and tropical storms (Carlson et al. 2010). Inshore of the 10 m isobaths, other factors affecting the flow (i.e., wave action, tidal currents,

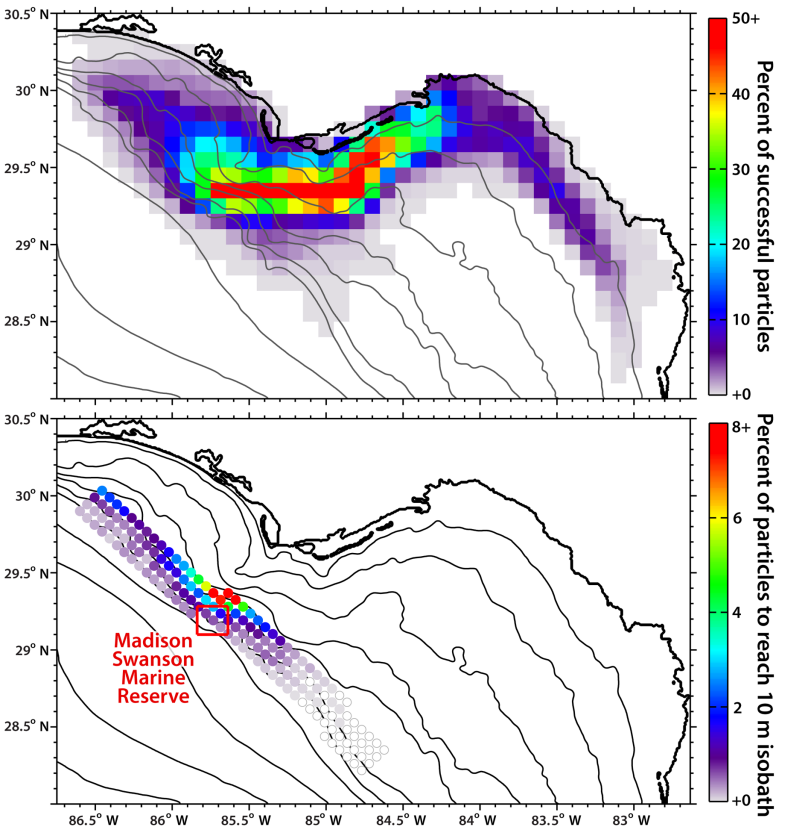

Figure 13. Particle track density of all particles that reached the 10 m isobath during their advection period (top) and the origins of particles that successfully reached the 10 m isobath during their advection (bottom). Circles are colored by the percentage of successful particles originating from that location, where open circles indicate zero particles to arrive inshore. Model bathymetry is contoured every 10 m until 50 m depth, then at depths of 75, 100, 200, 500, and 1,000 m.

and overlapping boundary layers) or gag larval behavior (such as settlement or lunar vertical migrations seen by Keener et al. [1988]) may have a significant impact on larval dispersal.

Particle track densities are calculated for only those ∼1% of particles that arrive at the 10 m isobath at some point during their advection (henceforth referred to as "successful" particles; Fig. 13). Most successful particles pass through the area immediately to the south of Cape San Blas and Cape St. George where percentages are 50%–80%. This is the same area with higher particle track densities in 2005 and 2010 (see Fig. 12c and h) and is an area that exhibits significant onshore flow in the mean circulation (see Figs. 7 and 8). Very few successful particles travel south of 28.8° N, demonstrating that the primary pathway

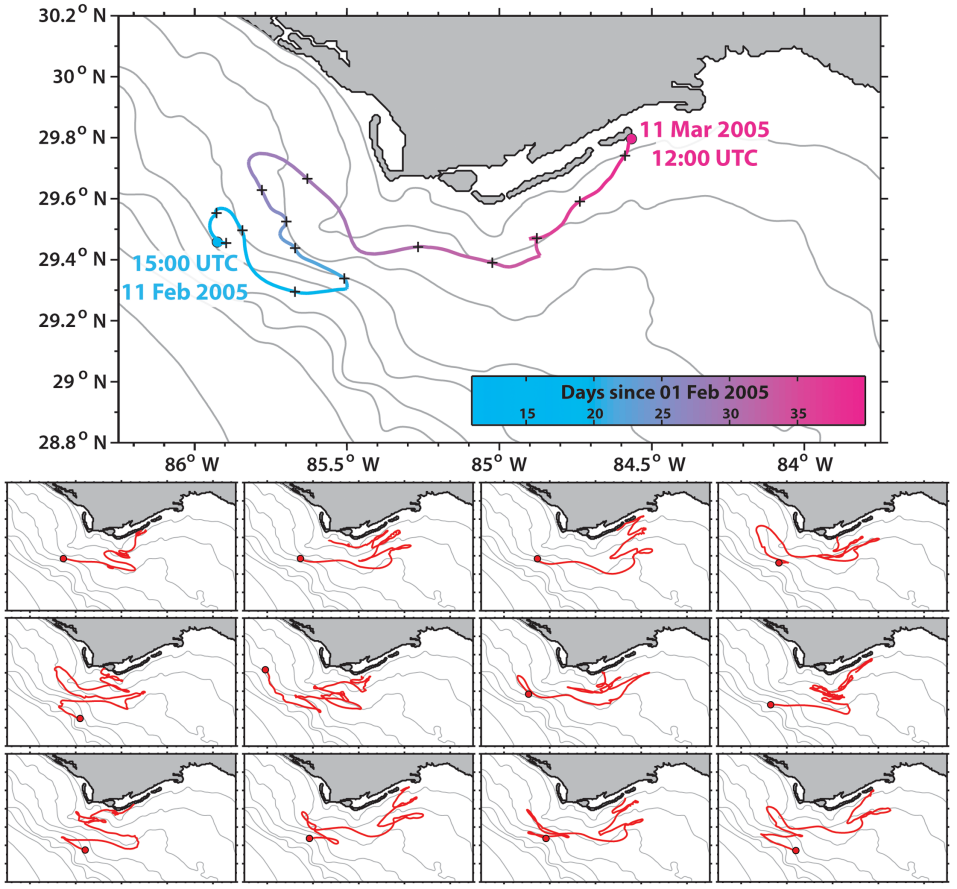

Figure 14. Trajectory of a particle released at 15:00 UTC on 11 February 2005 (top), where the color indicates the time during the particle's advection, and black crosses denote every second day from 13 March 2005 00:00 UTC. Thumbnails depict the paths of 12 other successful particles randomly selected from 2004 to 2010. Circles in the plots represent the starting location of each particle. Model bathymetry is contoured every 10 m until 50 m, then at depths of 75, 100, 200, and 500 m.

by which particles are able to reach inshore is via the region immediately south of Cape St. George, where there are two areas of onshore-directed mean velocities.

Consider particles flowing in the springtime circulation, which oscillates between phases of southeastward and northwestward flow (see Fig. 14 for the trajectory of one particle released at 15:00 UTC on 11 February 2005). Strong southeastward flow causes the particle to cross isobaths near Cape San Blas and Cape St. George (15–20 February in Fig. 14). Just before 21 February, the particle turns and moves along isobath in the weak northwestward flow (in water of shallower depth than where the particle was released on 11 February).

This oscillation in asymmetric flow patterns creates a ratcheting mechanism in which the particle crosses isobaths during one flow regime but moves along isobath in the other (this ratcheting is clearly visible in all the successful particle tracks displayed in Fig. 14). The timescale over which cross-isobath flow occurs (2–5 days) is less than the time over which frictional effects become important (3–15 days), justifying the hypothesis in Section 3c that the stronger southeastward flow is more nonlinear and is therefore able to cross isobaths. So, the presence of high successful particle track densities in the region with significant cross-isobath flow suggests that particles move back and forth across this area in conjunction with the oscillatory flow patterns, and transport to the inner shelf is only possible under a specific combination of oscillating synoptic-scale wind forcing.

Because very few successful particles travel south of 28.8° N during their advection, are particles that originate along the southern parts of the BBR shelf break capable of reaching the nearshore environment? That is, do significantly more successful particles originate from a particular area? Understanding these questions will facilitate the identification of potential preferred release locations for particles and, indeed, for gag larvae. The trajectories of particles are traced to estimate the percentage from each location that successfully reaches the 10 m isobath. Seeding locations that produce the highest percentage of successful particles are south of Cape San Blas, in the region of tightly curving isobaths where significant mean cross-isobath velocities are visible, and adjacent to the region of highest successful particle density (Fig. 13). The highest success rates indicate that more than 15% of all the particles released from this area arrive inshore of the 10 m isobath at some point during their 45-day advection. So, although only 1% of all the particles released across the domain arrive inshore, successful particles predominantly originate from this area offshore of Cape San Blas. In fact, particles released to the south of 28.8° N or to the west of 86.1° W are largely unsuccessful at reaching the nearshore region (no particles released south of 28.5° N ever arrive inshore).

c. Application to gag grouper

The plight of pelagic larvae is that they only survive if they are fortunate enough to avoid harsh marine environmental factors such as predation, lack of available food, intolerable temperatures or salinities, or failure to arrive in suitable nursery habitat (Norcross and Shaw 1984). This is evident because of the relatively small estimates of postlarval ingress observed in relation to the fecundity of adult gag (Keener et al. 1988) and is also supported by the BBROMS simulation results that 99% of the particles released within the domain never reach waters shallower than 10 m (where the vast majority of nursery habitat is found). So, although the percentage of particles that arrive within the 10 m isobath is low, this simply highlights the reliance of drifting particles on specific circulation features to provide their necessary transport inshore. Furthermore, the ability of these particles to arrive inshore can greatly depend on where they originate (Fig. 13). The region with the highest successful particle rates also coincides with a known gag spawning aggregation

site (the Madison Swanson Marine Reserve; Koenig et al. 2000). The colocation of the preferred release locations with a known gag spawning aggregation suggests that spawning site location could influence natural selection over time because of increased likelihood to be transported to the suitable nursery habitats of the BBR.

Annual fecundity estimates for individual adult gag in the BBR range from ~65,000 to 61.4 million and vary by size and by age of the fish (Collins et al. 1998). By assuming that the adult gag fecundity and the physical dispersal are the only variables that affect recruitment, these results indicate that gag spawning anywhere in the BBR shelf break could then see 650–614,000 successful recruits per spawning adult (at a 1% successful recruitment rate). However, gag spawning near the Madison Swanson Marine Reserve are 15 times more likely to arrive inshore, which corresponds to 9,750–9,210,00 successful recruits per spawning adult gag. These estimates reinforce the large range in variability in juvenile gag recruitment and demonstrate that spawning location could have a significant impact on recruitment success. Gag recruitment can be estimated by using the physical transport estimates together with larval mortality due to predation, environmental stressors, habitat suitability, and so forth.

5. Summary and discussion

The main flow features observed in the mean springtime BBR circulation include a northwestward-flowing slope jet, a southeastward-flowing coastal jet, and several areas of cross-shelf velocities offshore of Cape San Blas and Cape St. George. The slope jet flow toward the northwest is set primarily by the deep ocean, but the flow on the shelf is set by the large-scale, low-frequency wind stress and generally responds barotropically to these winds. The mean springtime velocities form a banded structure of offshore-directed flow adjacent to onshore-directed flow in the region with the most dramatic bathymetric curvature.

The hydrodynamic fields from the ocean model simulation are compared with several observation platforms across the region. The model simulation reproduces variations in sea level and surface temperatures that closely match the variability from observations at tide gauges ($R > 0.84$) or regional buoys ($R > 0.95$), respectively. When modeled velocities are compared with observed velocities at two different current meters located at depths of 19 m, the model captures the variability of subinertial velocities at both sites well ($R > 0.79$).

The mean shelf circulation in the BBR is composed almost entirely of flow during two opposing wind regimes: winds from the northwest and winds from the southeast. Winds with a westward component are much more frequent during the spring months, but southeastward winds are stronger. These stronger, yet less frequent, southeastward winds drive a correspondingly strong southeastward flow that is able to cross isobaths over regions with tight bathymetric curvature. Contrastingly, the flow during northwestward winds is more frequent but is generally weaker and able to more closely follow isobaths. The residual of these two asymmetric yet opposite oscillating flows is directed cross shore in the regions of tightly curving isobaths and is weak elsewhere.

The Lagrangian particle trajectories reveal the primary pathways of particles during their advection in the springtime circulation and provide notable improvements to the simple empirical model by Fitzhugh et al. (2005) by including the evolution of currents in time and space. Higher particle track densities along the shelf break illustrate that the primary pathway for advection is along the northwest-flowing slope jet, and shoreward advection occurs because of the cross-isobath flow during southeastward winds. There is considerable interannual variability in particle density patterns, particularly the distance that particles reach onshore. However, the cross-isobath movement is limited, and only a small percentage of particles make significant progress inshore. Years when higher percentages of particles are advected inshore correspond to years when the strength and width of mean cross-shelf current features are enhanced.

Fifty to eighty percent of successful particles travel immediately south of Apalachicola Bay at some point during their advection. This indicates that successful particles are carried inshore through this primary pathway to the south of Cape San Blas and Cape St. George and farther along isobath via the coastal jet. More particles follow this onshore tongue in the two positive ENSO-phase years within this study (2005 and 2010), indicating that the strength and sign of ENSO phase could have an impact on the magnitude of cross-shelf transport in the BBR by modulating the occurrence of springtime extratropical storms and their associated frontal passages over the gulf. However, a longer time record is needed to make any definitive conclusions regarding the impact of interannual to interdecadal oscillations on transport patterns in the BBR.

Roughly 50% of all the particles remain inside the model domain during their 45-day advection period, indicating that only $\sim$2% of the particles that remain inside the modeling domain arrive inshore. However, it is possible that more particles would have arrived inshore if their positions were able to be tracked over a larger domain or over longer timescales (say, the upper range of the gag pelagic larval duration, $\sim$60 days). Therefore, this work may actually underestimate the relative importance of this primary pathway or the percentage of particles that are able to arrive inshore.

Finally, a preferred origin for successful particles exists to the southwest of Cape San Blas. This preferred origin is immediately adjacent to the region of high successful particle density, to the locations where mean currents are directed cross isobath, and to a known gag spawning site. Overexploitation of fish species that form spawning aggregations (such as gag) can be reduced by establishing marine reserves (such as the Madison Swanson Marine Reserve; Coleman, Koenig, and Collins 1996; Koenig et al. 2000). However, the results presented in Section 4 suggest that the Madison Swanson Marine Reserve is also an important area because it is a preferred source region for transport into the shallow waters of the BBR. The location of this preferred origin for successful particles leads to some interesting biological questions, including whether this location is a preferred gag spawning aggregation site because it provides gag with the highest chance for their offspring to arrive in nursery habitats that are conducive for their survival. Simple estimates of recruitment using only the depth-averaged physical transport indicate that eggs released from gag near

the Madison Swanson Marine Reserve are 15 times more likely to arrive inshore than those originating elsewhere along the shelf break. The results presented in this study provide, for the first time, a description of the pathways capable of providing transport from adult gag spawning grounds at the shelf break to juvenile gag nursery habitats in the BBR.

Acknowledgments. This research was made possible by grants from the BP/The Gulf of Mexico Research Initiative to the Deep-C Consortium, NOAA's Northern Gulf Institute (12-NGI-33), the NASA/JPL Ocean Vector Winds Science Team (1419699), and the Office of Naval Research contract N00014-09-1-0587. The authors would also like to thank the Florida State University Current Meter Facility for the collection of observational data, Dr. Ekaterina Maksimova for her help processing this data, and Dr. Felicia Coleman for her insight into the ecology of the gag grouper.

REFERENCES

Barth, A., A. Alvera-Azcárate, and R. H. Weisberg. 2008a. Benefit of nesting a regional model into a large-scale ocean model instead of climatology. Application to the West Florida Shelf. Cont. Shelf Res., *28*, 561–573.

Barth, A., A. Alvera-Azcárate, and R. H. Weisberg. 2008b. A nested model study of the Loop Current generated variability and its impact on the West Florida Shelf. J. Geophys. Res.: Oceans, *113*, C05009. doi: 10.1029/2007JC004492

Beckman, A., and D. Haidvogel. 1993. Numerical simulation of flow around a tall isolated seamount. Part I: Problem formulation and model accuracy. J. Phys. Oceanogr., *23*, 1736–1753.

Bleck, R., 2002. An oceanic general circulation model framed in hybrid isopycnic-Cartesian coordinates. Ocean Modelling, *4*(1), 55–88.

Carlson, P. R., Jr., L. A. Yarbro, K. A. Kaufman, and R. A. Mattson. 2010. Vulnerability and resilience of seagrasses to hurricane and runoff impacts along Florida's west coast. Hydrobiologia, *649*, 39–53.

Chambers, R. C., and E. A. Trippel. 1997. Early Life History and Recruitment in Fish Populations. Dordrecht, The Netherlands: Springer, 632 pp.

Chapman, D. C. 1985. Numerical treatment of cross-shelf open boundaries in a barotropic coastal ocean model. J. Phys. Oceanogr., *15*, 1060–1075.

Chassignet, E. P. 2011. Isopycnic and hybrid ocean modeling in the context of GODAE, *in* Operational Oceanography in the 21st Century, A. Schiller and G. B. Brassington, eds. Dordrecht, The Netherlands: Springer, 263–293.

Chassignet, E. P., H. E. Hurlburt, E. J. Metzger, O. M. Smedstad, J. A. Cummings, G. R. Halliwell, R. Bleck, et al. 2009. US GODAE: Global ocean prediction with the HYbrid Coordinate Ocean Model (HYCOM). Oceanography, *22*(2), 64–75.

Chassignet, E. P., H. E. Hurlburt, O. M. Smedstad, G. R. Halliwell, P. J. Hogan, A. J. Wallcraft, R. Baraille, and R. Bleck. 2007. The HYCOM (HYbrid Coordinate Ocean Model) data assimilative system. J. Mar. Syst., *65*, 60–83.

Clarke, A. J., and K. H. Brink. 1985. The response of stratified, frictional flow of shelf and slope waters to fluctuating large-scale, low-frequency wind forcing. J. Phys. Oceanogr., *15*, 439–453.

Coleman, F. C., W. F. Figueira, J. S. Ueland, and L. B. Crowder. 2004. The impact of United States recreational fisheries on marine fish populations. Science, *305*, 1958–1960.

Coleman, F. C., C. C. Koenig, and L. A. Collins. 1996. Reproductive styles of shallow-water groupers (Pisces: Serranidae) in the eastern Gulf of Mexico and the consequences of fishing spawning aggregations. Environ. Biol. Fishes, *47*, 129–141.

Collins, L. A., A. G. Johnson, C. C. Koenig, and M. S. Baker, Jr., 1998. Reproductive patterns, sex ratio, and fecundity in gag, Mycteroperca microlepis (Serranidae), a protogynous grouper from the Northeastern Gulf of Mexico. Fishery Bulletin, *96*, 415–427.

Continental Shelf Associates Inc. 1987. Assessment of Hurricane Damage in the Florida Big Bend Seagrass Beds. Springfield, VA: U.S. Department of Commerce, National Technical Information Service, 95 pp.

Cummings, J. A. 2005. Operational multivariate ocean data assimilation. Q. J. R. Meteorol. Soc., *131*, 3583–3604.

Fairall, C. W., E. F. Bradley, J. E. Hare, A. A. Grachev, and J. B. Edson. 2003. Bulk parameterization of air-sea fluxes: Updates and verification for the COARE algorithm. J. Clim., *16*, 571–591.

Fitzhugh, G. R., C. C. Koenig, F. C. Coleman, C. B. Grimes., and W. Sturges. 2005. Spatial and temporal patterns in fertilization and settlement of young gag (*Mycteroperca microlepis*) along the West Florida Shelf. Bull. Mar. Sci., *77*(3), 337–396.

Flather, R.A. 1976. A tidal model of the northwest European continental shelf. Mem. Soc. R. Sci. Liege, *10*, 141–164.

Gentner, B. 2009. Allocation Analysis of the Gulf of Mexico Gag and Red Grouper Fisheries. Technical report. Houston, TX: Coastal Conservation Association, 27 pp.

Gouillon, F., S. L. Morey, D. S. Dukhovskoy, and J. J. O'Brien. 2010. Forced tidal response in the Gulf of Mexico. J. Geophys. Res.: Oceans, *115*, C10050. doi: 10.1029/2010JC006122.

Haney, R. L. 1991. On the pressure gradient force over steep topography in sigma coordinate ocean models. J. Phys. Oceanogr., *21*, 610–619.

He, R., and R. H. Weisberg. 2002a. Tides on the West Florida Shelf. J. Phys. Oceanogr., *32*, 3455–3473.

He, R., and R. H. Weisberg. 2002b. West Florida Shelf circulation and temperature budget for the 1999 spring transition. Cont. Shelf Res., *22*, 719–748.

He, R., and R. H. Weisberg. 2003. A Loop Current intrusion case study on the West Florida Shelf. J. Phys. Oceanogr., *33*, 465–477.

Hetland, R. D., Y. Hsueh, R. R. Leben, and P. P. Niiler. 1999. A Loop Current-induced jet along the edge of the West Florida Shelf. Geophys. Res. Lett., *26*(15), 2239–2242.

Hood, P. B., and R. A. Schlieder. 1992. Age, growth, and reproduction of gag, *Mycteroperca microlepis* (Pisces: Serranidae), in the eastern Gulf of Mexico. Bull. Mar. Sci., *51*, 337–352.

Iverson, R. L., and H. F. Bittaker. 1986. Seagrass distribution and abundance in Eastern Gulf of Mexico coastal waters. Estuarine, Coastal Shelf Sci., *22*, 577–602.

Kantha, L. H., and C. A. Clayson. 1994. An improved mixed layer model for geophysical applications. J. Geophys. Res.: Oceans, *99*, 25235–25266.

Keener, P., D. G. Johnson, B. W. Stender, E. B. Brothers, and H. R. Beatty. 1988. Ingress of postlarval gag *Mycteroperca microlepis* (Pisces: Serranidae), through a South Carolina barrier island inlet. Bull. Mar. Sci., *42*, 376–396.

Kennedy, A. J., M. L. Griffin, S. L. Morey, S. R. Smith, and J. J. O'Brien. 2007. Effects of El Niño–Southern Oscillation on sea level anomalies along the Gulf of Mexico coast. J. Geophys. Res.: Oceans, *112*, C05047. doi: 10.1029/2006JC003904

Koenig, C. C., and F. C. Coleman. 1998. Absolute abundance and survival of juvenile gags in sea grass beds of the northeastern Gulf of Mexico. Trans. Am. Fish. Soc., *127*, 44–55.

Koenig, C. C., F. C. Coleman, C. B. Grimes, G. R. Fitzhugh, K. M. Scanlon, C. T. Gledhill, and M. Grace. 2000. Protection of fish spawning habitat for the conservation of warm-temperate reef-fish fisheries of shelf-edge reefs of Florida. Bull. Mar. Sci., *66*, 593–616.

Lemarié, F., J. Kurian, A. F. Shchepetkin, M. J. Molemaker, F. Colas, and J. C. McWilliams. 2012. Are there inescapable issues prohibiting the use of terrain-following coordinates in climate models? Ocean Modell., *42*, 57–79.

Maksimova, E. V., and A. J. Clarke. 2013. Multiyear subinertial and seasonal Eulerian current observations near the Florida Big Bend coast. J. Phys. Oceanogr., *43*, 1691–1709.

Marchesiello P. L. Debreu and X. Couvelard. 2009. Spurious diapycnal mixing in terrain-following coordinate models: the problem and a solution. Ocean Modelling, *26*, 156–169.

Marchesiello, P., J. C. McWilliams, and A. Shchepetkin. 2001. Open boundary condition for long-term integration of regional oceanic models. Ocean Modell., *3*, 1–20.

Marmorino, G. O. 1983a. Summertime coastal currents in the northeastern Gulf of Mexico. J. Phys. Oceanogr., *13*, 65–77.

Marmorino, G. O. 1983b. Variability of current, temperature, and bottom pressure across the west Florida continental shelf, winter 1981–1982. J. Geophys. Res.: Oceans, *88*(C7), 4439–4457.

Mellor, G. L., and T. Yamada. 1974. A hierarchy of turbulence closure models for planetary boundary layers. J. Atmos. Sci., *31*, 1791–1806.

Mellor, G. L., and T. Yamada. 1982. Development of a turbulence closure model for geophysical fluid problems. Rev. Geophys., *20*, 851–875.

Mitchum, G. T., and A. J. Clarke. 1986. Evaluation of frictional, wind-forced long-wave theory on the West Florida Shelf. J. Phys. Oceanogr., *16*, 1029–1037.

Mitchum, G. T., and W. Sturges. 1982. Wind-driven currents on the West Florida Shelf. J. Phys. Oceanogr., *12*, 1310–1317.

Morey, S. L., D. S. Dukhovskoy, and M. A. Bourassa. 2009. Connectivity between variability of the Apalachicola River flow and the biophysical oceanic properties of the northern West Florida Shelf. Cont. Shelf Res., *29*, 1264–1275.

Morey, S. L., and J. J. O'Brien. 2002. The spring transition from horizontal to vertical thermal stratification on a midlatitude continental shelf. J. Geophys. Res.: Oceans, *107*(C8). doi: 10.1029/2001JC000826

Morey, S. L., J. Zavala-Hidalgo, and J. J. O'Brien. 2005. The seasonal variability of continental shelf circulation in the northern and western Gulf of Mexico from a high-resolution numerical model, *in* Circulation in the Gulf of Mexico: Observations and Models, W. Sturges and A. Lugo-Fernandez, eds. Geophysical Monograph Series, vol. 161. Washington, D.C.: American Geophysical Union, 203–218.

Norcross, B. L., and R. F. Shaw. 1984. Oceanic and estuarine transport of fish eggs and larvae: A review. Trans. Am. Fish. Soc., *113*, 153–165.

North, E. W., Z. Schlag, R. R. Hood, M. Li, L. Zhong, T. Gross, and V. S. Kennedy. 2008. Vertical swimming behavior influences the dispersal of simulated oyster larvae in a coupled particle-tracking and hydrodynamic model of Chesapeake Bay. Mar. Ecol.: Prog. Ser., *359*, 99–115.

Pedlosky, J. 1987. Geophysical Fluid Dynamics, 2nd ed. New York: Springer-Verlag, 710 pp.

Rothschild, B. J. 1986. Dynamics of Marine Fish Populations. Cambridge, MA: Harvard University Press, 277 pp.

Rothschild, B. J., and T. R. Osborn. 1988. Small-scale turbulence and plankton contact rates. J. Plankton Res., *10*, 465–474.

Saha, S., S. Nadiga, C. Thiaw, J. Wang, W. Wang, Q. Zhang, H. M. Van den Dool, et al. 2006. The NCEP Climate Forecast System. J. Clim., *19*, 3483–3517.

Schlag, Z., E. W. North, and K. Smith. 2008. Larval TRANSport Lagrangian Model (LTRANS) User's Guide. Cambridge, MD: University of Maryland Center for Environmental Science, Horn Point Laboratory, 146 pp.Shchepetkin, A. F., and J. C. McWilliams. 1998. Quasi-monotone advection schemes based on explicit locally adaptive dissipation. Mon. Weather Rev., *126*, 1541–1580.

Shchepetkin, A. F., and J. C. McWilliams. 2003. A method for computing horizontal pressure-gradient force in an oceanic model with a nonaligned vertical coordinate. J. Geophys. Res.: Oceans, *108*(C3), 3090. doi: 10.1029/2001JC001047

Shchepetkin, A. F., and J. C. McWilliams. 2005. The regional oceanic modeling system (ROMS): A split-explicit, free-surface, topography-following-coordinate oceanic model. Ocean Modell., *9*, 347–404.

Sikirić, M. D., I. Janeković, and M. Kuzmić. 2009. A new approach to bathymetry smoothing in sigma-coordinate ocean models. Ocean Modell., *29*, 128–136.

Smith, S. R., P. M. Green, A. P. Leonardi, and J. J. O'Brien. 1998. Role of multiple-level tropospheric circulations in forcing ENSO winter precipitation anomalies. Mon. Weather Rev., *126*, 3102–3116.

Smolarkiewicz, P. K. 1984. A fully multidimensional positive definite advection transport algorithm with small implicit diffusion. J. Comput. Phys., *54*, 325–362.

Thompson, M. J., and N. W. Phillips. 1987. Assessment of Hurricane Damage in the Florida Big Bend Seagrass Beds. New Orleans, LA: U.S. Department of the Interior/Minerals Management Service, 95 pp.

Weatherly, G. L., and D. Thistle. 1997. On the wintertime currents of the Florida Big Bend region. Cont. Shelf Res., *17*, 1297–1319.

Weatherly, G. L., N. Wienders, and A. Romanou. 2005. Intermediate-depth circulation in the Gulf of Mexico estimated from direct measurements, *in* Circulation in the Gulf of Mexico: Observations and Models, W. Sturges and A. Lugo-Fernandez, eds. Geophysical Monograph Series, vol. 161. Washington, D.C.: American Geophysical Union, 315–324.

Weisberg, R. H., and R. He. 2003. Local and deep-ocean forcing contributions to anomalous water properties on the West Florida Shelf. J. Geophys. Res.: Oceans, *108*(C6), 3184. doi: 10.1029/2002JC001407

Weisberg, R. H., R. He, Y. Liu, and J. I. Virmani. 2005. West Florida Shelf circulation on synoptic, seasonal, and interannual time scales, *in* Circulation in the Gulf of Mexico: Observations and Models, W. Sturges and A. Lugo-Fernandez, eds. Geophysical Monograph Series, vol. 161. Washington, D.C.: American Geophysical Union, 325–347.

Werner, F. E., J. A. Quinlan, B. O. Blanton, and R. A. Luettich Jr. 1997. The role of hydrodynamics in explaining variability in fish populations. J. Sea Res., *37*, 195–212.

Yang, H., and R. H. Weisberg. 1999. Response of the West Florida Shelf circulation to climatological wind stress forcing. J. Geophys. Res.: Oceans, *104*(C3), 5301–5320.

Yang, H., R. H. Weisberg, P. P. Niiler, W. Sturges, and W. Johnson. 1999. Lagrangian circulation and the forbidden zone on the West Florida Shelf. Cont. Shelf Res., *19*, 1221–1245.

Received: *6 August 2013*; revised: *24 November 2014*.